ACS EARTH AND SPACE CHEMISTRY

Article

http://pubs.acs.org/journal/aesccq

Electron Mobility and Trapping in Ferrihydrite Nanoparticles

Jennifer A. Soltis,[†,‡] Adam M. Schwartzberg,[§] Piotr Zarzycki,[⊥,∥] R. Lee Penn,[†] Kevin M. Rosso,[*,‡] and Benjamin Gilbert[*,⊥]

[†]Department of Chemistry, University of Minnesota, Minneapolis, Minnesota 55455, United States

[‡]Physical Sciences Division, Pacific Northwest National Laboratory, Richland, Washington 99354, United States

[§]Molecular Foundry and [⊥]Earth Sciences Division, Lawrence Berkeley National Laboratory, Berkeley, California 94720, United States

[∥]Institute of Physical Chemistry, Polish Academy of Sciences, 01-224 Warsaw, Poland

ABSTRACT: Iron is the most abundant transition metal in the Earth's crust, and naturally occurring iron oxide minerals play a commanding role in environmental redox reactions. Although iron oxide redox reactions are well-studied, their precise mechanisms are not fully understood. Recent work has shown that these involve electron transfer pathways within the solid, suggesting that overall reaction rates could be dependent upon electron mobility. Initial ultrafast spectroscopy studies of iron oxide nanoparticles sensitized by fluorescein derivatives supported a model for electron mobility based on polaronic hopping of electron charge carriers between iron sites, but the constitutive relationships between hopping mobilities and interfacial charge transfer processes has remained obscured. We developed a coarse-grained lattice Monte Carlo model to simulate the collective mobilities and lifetimes of these photoinjected electrons with respect to recombination with adsorbed dye molecules for essential nanophase ferrihydrite and tested predictions made by the simulations using pump−probe spectroscopy. We acquired optical transient absorption spectra as a function of the particle size and under a variety of solution conditions and used cryogenic transmission electron microscopy to determine the aggregation state of the nanoparticles. We observed biphasic electron recombination kinetics over time scales that spanned from picoseconds to microseconds, the slower regime of which was fit with a stretched exponential decay function. The recombination rates were weakly affected by the nanoparticle size and aggregation state, suspension pH, and injection of multiple electrons per nanoparticle. We conclude that electron mobility indeed limits the rate of interfacial electron transfer in these systems, with the slowest processes relating to escape from deep traps, the presence of which outweighs the influence of environmental factors, such as pH-dependent surface charge.

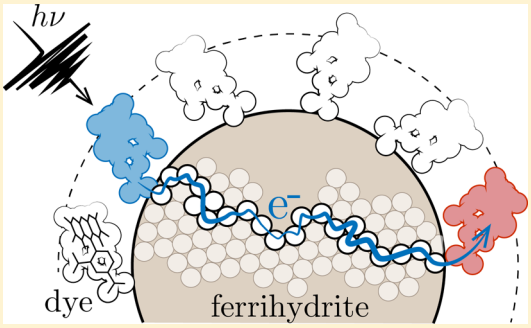

KEYWORDS: *iron, redox, electron transfer, ferrihydrite, charge separation*

INTRODUCTION

Iron oxide, hydroxide, and oxyhydroxide minerals (collectively referred to as iron oxides) are abundant in soils, groundwater, and marine environments.[1−4] They play important roles in biogeochemical cycling of many elements due, in part, to their redox reactivity. Ferrihydrite, a nanophase and poorly crystalline Fe(III) oxyhydroxide, plays an especially important role in controlling contaminant and nutrient availability.[1,2,4,5] Arsenic, aluminum, and heavy metals can be adsorbed to or incorporated into ferrihydrite, sequestering them from the water supply.[6−11] However, iron oxides readily undergo reductive transformations under appropriate conditions, altering the bioavailability of iron and such associated species.[12−15]

The factors controlling the environmental reactivity of iron oxide nanoparticles have been examined by several groups. The rate of reductive dissolution can change based on the particle size, crystallinity, reactive surface area,[14] and inclusion of other metals.[13,16,17] Temperature-dependent studies found that the activation energy and rate-determining step in reductive dissolution of ferrihydrite did not change as a function of the particle size,[14] arsenic doping,[13] or differences in structure or composition.[13] However, the rate and activation energy for reductive dissolution were influenced by surface-bound As[12,13,18] and the amount of aluminum substitution in Al-doped particles.[12,16,17] The interpretation of these disparate observations and the establishment of a basis for predicting iron oxide reactivity require knowledge of the molecular mechanism for the process.

A widely accepted mechanism for the reductive dissolution of iron(III) oxide involves sorption of the electron donor, interfacial electron transfer, and release of the oxidized donor followed by the reduced iron(II) atom.[15] However, there is now abundant evidence that, despite high resistivities, electrons transferred to iron(III) oxides are mobile within the crystal lattice. This behavior is explained by the small polaron model, in which an electron charge carrier is self-trapped at an iron site through a local lattice relaxation. This localized charge/distortion quasi-

Received: March 23, 2017
Revised: May 8, 2017
Accepted: May 18, 2017
Published: May 18, 2017

DOI: 10.1021/acsearthspacechem.7b00030
ACS Earth Space Chem. XXXX, XXX, XXX−XXX

particle can move through the lattice by thermally activated nearest neighbor hopping. Recently, Katz et al. reported ultrafast optical and X-ray studies of iron oxide nanoparticles that were sensitized by a fluorescein dye.[19] That work supported the small polaron model and demonstrated electron hopping rates on a sub-nanosecond time scale, finding good agreement with predictions from simulation.

This mobility of charge-carrying electrons in iron oxides can have striking consequences. For example, exposure of magnetite and goethite nanoparticles to aqueous iron(II) leads to rapid atom exchange without a net redox reaction.[20−22] Yanina and Rosso demonstrated that solid-state electron transport could couple redox reactions occurring on two different faces of hematite.[23] Earlier studies of iron oxide reduction using pulse radiolysis concluded that electron migration could cause indefinite trapping of electrons.[24] Thus, internal electron conduction could contribute to the overall reaction rates of iron oxide dissolution or recrystallization, but this contribution has never been quantified.

Our prior work using dye-sensitized iron oxides showed that, although a portion of the electrons transferred to iron oxide returned to the electron donor molecule within ∼3 ns, a significant fraction remained within the nanoparticles for longer (i.e., at least microsecond) time scales. We postulated that accurate quantification of the longer time scale kinetics for recombination would allow for testing of models for electron mobility within iron oxides, thereby linking single electron-transfer steps to overall electron fluxes across the particle−dye interface and ultimately the rate of observable reactions. As precedence for this approach, quantification of injected electron signals in TiO_2 nanoparticles over microsecond and longer time scales was used to develop a mechanism for electron mobility in nanocrystalline electrodes that could predict device performance.[25]

We developed a coarse-grained lattice Monte Carlo (MC) simulation to mimic the collective site-to-site diffusion dynamics of multiple electron polarons on a cubic lattice of a spherical particle. The model established two testable hypotheses that motivated the experimental design. First, the MC simulations clearly demonstrated a scenario in which a fraction of injected electrons were dynamically trapped within the nanoparticles and underwent slow recombination at rates that were determined by a random walk within the nanoparticle interior and impingement on surface dye-bound sites. This suggested that the recombination kinetics would exhibit a dependence upon the particle size. Second, the incorporation of a treatment of electrostatic interactions in the particles indicated that the electron trajectories could be electrostatically biased by the pH-dependent net surface charge through its control of the inner Helmholtz potential. Because iron oxide surfaces undergo protonation/deprotonation reactions as a function of pH, the simulation predicts that electron trajectories and, thus, the recombination rate should be pH-dependent.

We tested these hypotheses using optical transient absorption (TA) to quantify the lifetimes of electrons transferred to dye-sensitized ferrihydrite nanoparticles as a function of the particle size and solution pH, a parameter that also requires the role of the aggregation state to be examined. Penn and co-workers have developed a synthesis method that is proven to generate six-line ferrihydrite nanoparticles with mean diameters that can be tuned by synthesis conditions.[26] These materials have been used in many prior studies of the ferrihydrite structure and reactivity.[13,16,26−34] Because electron charge carriers in ferrihydrite do not have a strong optical signature, the recombination rate was quantified by monitoring the signal from the oxidized state of the surface-bound dye molecule.[35]

By deducing electron recombination rates from the sub-picosecond time scale up to 400 μs as a function of the particle size and solution conditions, our work compellingly shows that the slowest recombination rates arise from injected electrons bound in deep trap states and that the presence of these deep traps outweighs the influence of environmental conditions at the interface. Longest lived injected electrons are trapped at unknown sites within 1 μs, and the rates of subsequent redox processes are likely dominated by rates of deep trap escape. This work is an important additional step toward the determination of the chemical and structural controls on a mineral redox reaction.

MATERIALS AND METHODS

American Chemical Society (ACS)-grade chemicals were purchased from Sigma-Aldrich or Fisher. Two sensitizer dyes, 2′,7′-dichlorofluorescein (27DCF) and 5(6)-carboxy-2′,7′-dichlorofluorescein (CDCF), were purchased from Sigma-Aldrich. All solutions and suspensions were prepared with deoxygenated ultrapure water (18 MΩ) in a glovebox with a $N_{2(g)}$ + 5% $H_{2(g)}$ atmosphere.

Nanoparticle Synthesis. Ferrihydrite nanoparticles were synthesized following the procedure of Burleson and Penn.[26] Sodium bicarbonate (0.48 M) was added via a peristaltic pump to an equal volume of 0.40 M ferric nitrate, with stirring, for a total addition period of 8−10 min. Particles were synthesized at 1, 40, and 80 °C using ice or hot water baths as needed, and all solutions were allowed to come to equilibrium temperature before synthesis began. Samples are named to indicate their synthesis temperature in degrees Celsius. For example, FHyd40 was synthesized at 40 °C. After the addition of base was complete, the nanoparticle suspensions were stirred for an additional 3 min. The 40 and 80 °C suspensions were then rapidly brought to room temperature in an ice bath. A microwave anneal step was performed as detailed by Burleson and Penn.[26] The suspensions were again brought to room temperature in an ice bath and placed in dialysis tubing [Spectra-Por 7 dialysis tubing, molecular weight cut-off (MWCO) = 2000 g/mol]. The nanoparticles were dialyzed against ultrapure water for a total of nine water changes over several days. The minimum time interval between water changes was 3 h, and all samples were stored at 10 °C during dialysis to slow transformation to other mineral phases. Many surface oxygen sites on ferrihydrite can undergo protonation/deprotonation reactions, leading to a permanent positive surface charge for pH values below the point of zero surface charge (pH_{zsc}).[36] Prior work with ferrihydrite nanoparticles that were synthesized using the same approach showed pH_{zsc} 8.6.[37]

Nanoparticle Characterization. *Mass Loading.* Mass loading of nanoparticles was determined by drying 1.000, 2.000, 5.00, and 10.00 mL of each suspension and massing the dried samples. The mass of the dry nanoparticles was plotted as a function of the suspension volume and fit with a linear trendline with a forced y intercept of zero. Mass loading in milligrams per milliliter was taken from the slope of this line.

X-ray Diffraction (XRD). Dried nanoparticles were ground with an agate mortar and pestle in preparation for XRD characterization. Samples were front-packed into a zero-background quartz holder. XRD patterns were collected using a PANalytical X'Pert Pro MPD θ−θ diffractometer with a cobalt Kα source and an X'Celerator detector over the range of 20−80°

DOI: 10.1021/acsearthspacechem.7b00030
ACS Earth Space Chem. XXXX, XXX, XXX−XXX

2θ and compared to the International Centre for Diffraction Data reference powder diffraction file for six-line ferrihydrite (29-712).

Particle Sizing. One drop of diluted FHyd suspension was placed onto a 200 mesh Cu holey carbon grid (Structure Probe, Inc.) and allowed to dry. Nanoparticle lengths were measured from calibrated transmission electron microscopy (TEM) images collected on a FEI Tecnai T12 with a LaB_6 source operating at 120 kV using a Gatan charge-coupled device (CCD) camera. Images were processed with a Gatan DigitalMicrograph, version 3.8.2. ImageJ was used to measure the lengths of 200−275 nanoparticles for each synthesis temperature. ImageJ is a public domain image processing and analysis program written by Wayne S. Rasband at the National Institutes of Health (NIH, Bethesda, MD, U.S.A.).[38] An aspect ratio of 1.3 was assumed for all FHyd particles based on measurements of both length and width taken in a previous work.[39]

Cryogenic Transmission Electron Microscopy (Cryo-TEM). Cryo-TEM specimens were prepared on a Vitrobot (FEI Mark III). Cu lacy carbon grids (200 mesh, Structure Probe, Inc.) were charged in a Pelco glow discharger for 60 s. A total of 3 μL of suspension was placed onto an individual grid and blotted with filter paper for 1 s. The grid was then plunged into liquid ethane (−183 °C) and transferred to a storage box under liquid nitrogen (−178 °C). All subsequent handling of the prepared grids occurred under liquid nitrogen to maintain cryogenic conditions. Samples were imaged on FEI Tecnai G^2 Spirit BioTWIN TEM with a LaB_6 source, equipped with a cryo stage and Eagle 2k CCD camera and operated at 120 keV.

Ultraviolet−Visible (UV−Vis) Spectroscopy. UV−vis spectroscopy was performed on an Ocean Optics USB4000 spectrometer using the SpectraSuite 2.0 software (Ocean Optics). Ferrihydrite nanoparticle mass loadings for all UV−vis and TA spectroscopies were chosen to maintain an optical density (OD) of 0.7 absorption units at 430 nm in 2 mm path length quartz cuvettes for unsensitized (dye-free) particles and ranged from 0.700 to 0.944 mg/mL, depending upon the particle size.

Dye Sensitization. The ferrihydrite nanoparticles were sensitized by quickly adding a 1 mL suspension of nanoparticles at a mass loading of 0.700−0.944 mg/mL (depending upon the particle size) and pH 4 to a 1.7 mL vial containing a small volume (5−100 μL) of a 2.5 mM stock solution of sensitizer dye at pH 9. This method generated a suspension of sensitized nanoparticles with a final pH between 3.75 and 4.1, depending upon the amount of dye added. Representative UV−vis absorption spectra for FHyd40 nanoparticles sensitized by 27DCF and CDCF are given in Figure 1.

We found it challenging to prepare stable suspensions of 27DCF-sensitized nanoparticles at pH values different from pH 4. At lower pH, the dye desorbed from the surface. This effect was reduced using the closely related dye, CDCF, which exhibited higher affinity to ferrihydrite and was more stable at lower pH. At higher pH, the suspensions aggregated, causing very poor TA data quality. This effect was slightly reduced using the lowest possible dye coverage (equivalent to ∼10% maximum coverage). To achieve a different final pH, a small amount of either 4 M NaOH (1−5 μL) or 2 M HCl (1−4 μL) was added to either the dye solution or nanoparticle suspension, respectively, prior to mixing.

Using CDCF as the sensitizer dye and a low surface coverage, we were able to prepare stable, non-aggregated suspensions covering a range of over 2.5 pH units (2.9−5.5). Although this

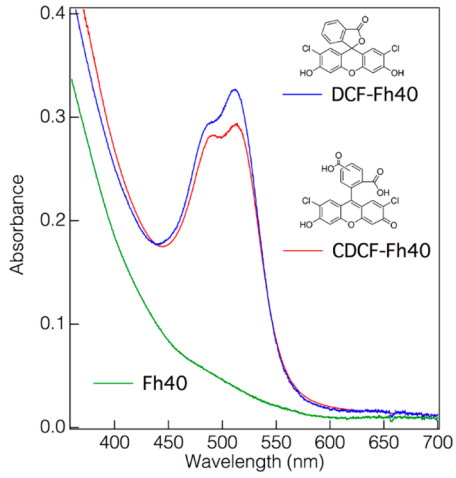

Figure 1. UV−vis absorption spectra of 27DCF (blue) and CDCF (red) bound to ferrihydrite nanoparticles (sample FHyd40) and measured at pH 4. The UV−vis spectrum of uncoated Fh40 is also shown (green).

lies substantially below pH_{zsc}, it corresponds to a large change in surface charge density, from approximately 1.3 to 0.4 $\mu C/cm^2$.[37]

Optical TA Spectroscopy. Optical TA experiments were carried out on a HELIOS femtosecond TA spectrometer and on an EOS sub-nanosecond TA spectrometer from Ultrafast systems installed at the Molecular Foundry, Lawrence Berkeley National Laboratory, Berkeley, CA, U.S.A. The laser source for both instruments was a Coherent Libra amplified femtosecond laser system operating at 1 kHz with 45 fs pulse duration. The laser output was split, with one arm passing through a Coherent OPerA optical parametric amplifier (OPA) to produce tunable pump pulses and the other arm delivered to the TA system, where a white-light probe pulse was generated in a sapphire plate or by a fiber white light source (Leukos-STM) for the HELIOS and EOS spectrometers, respectively. The pump pulse used in our measurements was tuned to 520 nm. The intensity of the pump beam was measured by a portable power meter (Vega P/N 7Z01560, Ophir Optronics) and was 7.5 μJ, except where otherwise stated. Time delay was provided by a mechanical delay stage for the HELIOS setup and by instrument electronics on the EOS setup. Spectra were collected in the UV−vis range between 300 and 900 nm.

All samples were kept in aqueous suspension and stored and handled anaerobically prior to analysis. The anaerobic samples were not exposed to air until analysis but were measured and stored as aerobic samples during and after spectroscopic experiments. For nanosecond TA studies, the samples were analyzed in 2 mm path length stoppered quartz cuvettes while stirring with a magnetic stir bar. For microsecond TA studies, approximately 10 mL of suspension was recirculated in a 2 mm path length flow-through quartz cuvette.

The spectra were collected from −10 ps to 8 ns (relative to the pump pulse arrival) on the HELIOS system and from 1 ns to 40 or 400 μs on the EOS system. Custom user routines developed in the IgorPro software (WaveMetrics, Inc., Lake Oswego, OR, U.S.A.) were used to process the data, to correct the time-dependent frequency modulation of the laser (chirp) on the signal to within ∼150 fs and to extract transient kinetic data at 418 and 447 nm from two-dimensional (2D) plots of spectra versus time.

Fitting the Transient Kinetics. The TA kinetics at a single wavelength (447 nm) were fitted using routines written in

DOI: 10.1021/acsearthspacechem.7b00030
ACS Earth Space Chem. XXXX, XXX, XXX−XXX

IgorPro. The sub-nanosecond regime was modeled as a sum of exponential decay functions. We investigated two approaches to model the nanosecond−millisecond regime. We first implemented a multiplicative power law decay but found that this function could not adequately reproduce the data without an additional arbitrary intensity offset. Instead, we obtained adequate agreement using a single stretched exponential for the microsecond time scale data. Stretched exponential responses are observed in numerous systems, including ultrafast electron-transfer processes in solids,[40,41] and may indicate that the observed dynamics are a sum of exponential decay processes with a range of time constants.[42] The TA kinetic response is then written as

$$\mathrm{TA}(t) = a_j \exp(-t/\tau_j)^{\beta} + \sum_i a_i \exp(-t/\tau_i) \quad (1)$$

where a_i and τ_i are the amplitude and time constants, respectively, for the ith exponential decay, and τ_j and β are the time constant and stretching exponent, respectively, for the single stretched exponential and where $0 \leq \beta \leq 1$. For fits to the EOS nanosecond−millisecond data, only the single stretched exponential was used.

As described below, we found the rates of recombination to be very similar for all samples studied. Several attempts were made to fit the data in a consistent manner to allow trends to be revealed. While the stretched exponential provided a suitable functional form, the time constant τ_j was frequently not stably fitted, because its best fit numerical value was close to or below the low end of the fit range. Therefore, we fixed τ_j at 0.1 μs and fitted a_j and β only. A smaller value of β causes longer tails of the stretched exponential and, hence, indicates a slower recombination rate.

Calculating the Dye Photoexcitation Efficiency. We estimated the fraction of adsorbed dye molecules that were photoexcited per laser pulse as a function of the pulse energy. On the basis of the ground-state UV−vis data (Figure 1), we assumed that only ∼50% of the incident light at 520 nm was available for dye excitation because of losses to bandgap excitations of the nanoparticles. Electron−hole pairs generated by bandgap excitation recombined within ∼300 ps[35] and were not detectable in the present microsecond TA experiments. The UV−vis data showed that there was no unbound dye in solution; therefore, all of the photoexcited dye molecules were adsorbed to nanoparticle surfaces and were potential electron donors. Light scattering effects were neglected. Because a high fraction of the dye molecules were excited, we used a numerical approach to simulate the propagation of photons through the suspension, calculating the differential loss of photons over ∼2 μm steps. To estimate the number of electrons injected per nanoparticle, we assumed the probability for interfacial electron transfer from a photoexcited dye molecule to be unity.

Lattice MC Simulations of Electron Propagation and Recombination. We implemented a lattice MC model to investigate plausible mechanisms that caused long time scale trapping of electrons transferred to a nanoparticle. An iron oxide nanoparticle was represented in the MC model as a 3.4 nm sphere containing a cubic lattice of iron sites. The lattice was populated with electrons according to one of two different random initial distributions: at any site or at near-surface sites. Self-diffusion of hopping electrons was treated as a thermally activated electron exchange reaction between one occupied and one neighboring unoccupied iron site. A Metropolis acceptance rule determined the probability of exchange between sites for which the electron affinity was calculated using one of three models for the interior electrostatic potential described below.[43] Loss of self-diffusing electrons occurred at the surface sites that are assigned randomly as electron exit channels (e.g., representing adsorbed oxidized dye molecules) at the beginning of simulations in a number equal to the number of injected electrons. These "exit channels" were closed following electron loss, representing recombination with a surface-bound oxidized dye molecule. The results of 100 MC simulations were averaged.[36]

A key aspect of metal oxide nanoparticles is the presence of a positive surface potential arising from the predominance of surface protonated groups expected at the pH value of the experiment (pH 4; ferrihydrite point of zero net surface charge (zsc) $\mathrm{pH_{zsc}}$ 8.6), the presence of surface-bound positively charged oxidized dye molecules, or both. Therefore, we incorporated the external electrostatic influences on electron self-diffusion in the solid, the trajectory of which would otherwise be characterized as a random three-dimensional walk restricted to nearest neighbor exchanges and single-site occupation. Transient electrons in the solid were treated as electronegative ($-1e$ net charge) and electrostatically attracted to the positive surface potential (when applied). The simulation computed the gradient of the electrostatic potential radially distributed inside the nanoparticle and applied this potential as a bias on the random walk of self-diffusing electrons. Two methods were used to compute the electrostatic potential: one based on solving the Poisson equation and another based on a simple electrostatic screening equation. The time-dependent electrostatic bias for electron self-diffusion was solved on-the-fly at each MC step using the following form of the Poisson equation:

$$\frac{1}{r^2}\frac{\partial}{\partial r}\left(r^2\frac{\partial}{\partial r}\right)\psi(r) = \frac{e}{\varepsilon_0\varepsilon_s}n_e(r) \quad (2)$$

where $\psi(r)$ and $n_e(r)$ are the electrostatic potential and electron density at a given radius from the nanoparticle center (charge density), respectively, e is the elementary charge, and ε_0 and ε_s are the vacuum permittivity and relative dielectric constant of maghemite (ε_s = 10.2), a bulk analogue for ferrihydrite, respectively. To solve this second-order ordinary differential equation, we applied the following boundary conditions for the nanoparticle surface ($r = r_s$):

$$\psi(r = r_s) = \psi_0 \quad (3a)$$

$$-\frac{\partial}{\partial r}\psi(r)\Big|_{r=r_s} = \frac{\psi_0}{r_s} + \psi_0\kappa \quad (3b)$$

where ψ_0 is the surface potential, whose pH dependence is approximated by the quasi-Nernst equation[43,44]

$$\psi_0 = \lambda\frac{2.303k_BT}{e}(\mathrm{PZP} - \mathrm{pH}) \quad (4)$$

where PZP is the point of zero potential [taken as the point of zero charge (PZC)] and λ describes the deviation of the surface potential response to the change in the bulk pH with respect to the Nernst response ($\lambda = 0.9$). The condition for the electrostatic field at the nanoparticle surface ($-\psi'$) is derived assuming that the double electrical layer formed at the nanoparticle interface with solution can be approximated by the Gouy−Chapman theory (i.e., as a diffuse electrical layer). Parameter K is the inverse Debye screening parameter that describes the electrical double layer thickness and is calculated assuming a simple 0.1

DOI: 10.1021/acsearthspacechem.7b00030
ACS Earth Space Chem. XXXX, XXX, XXX−XXX

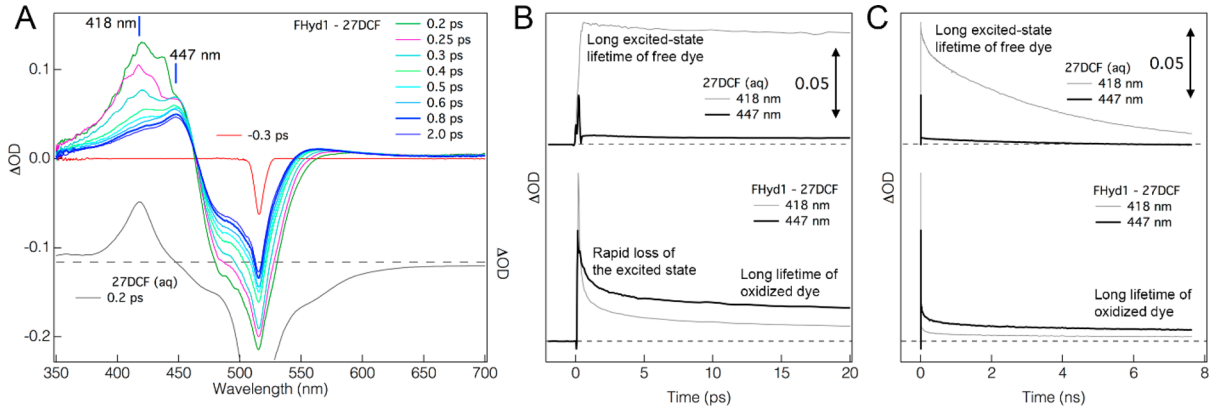

Figure 2. Optical TA analysis of the photoexcitation of free and bound 27DCF. (A) TA spectra taken before (−0.3 ps) and after 520 nm laser excitation of 27DCF bound to FHyd1 compared to the TA spectrum of aqueous 27DCF at 0.2 ps after excitation. The TA spectra are displayed as the mathematical subtraction of the ground-state spectrum from the time-dependent spectrum. (B) Comparison of the TA kinetics at 417 and 447 nm for dissolved (top) and bound (bottom) 27DCF on the picosecond time scale. (C) Comparison of the TA kinetics on the nanosecond time scale.

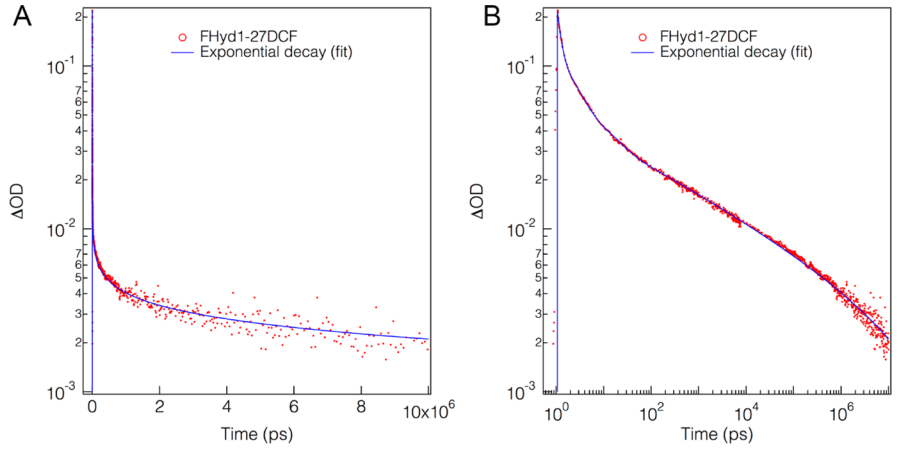

Figure 3. Optical TA signal at 447 nm for 27DCF-sensitized FHyd1 nanoparticles shown on a (A) linear and (B) logarithmic time axis. The plot displays data from equivalent samples acquired on two instruments with different time resolutions. The fit includes three exponential decays and a single stretched exponential. The time axis in panel B was shifted to place time zero at 1 ps and enable plotting on a logarithmic axis.

mol/dm^3 electrolyte (1:1). The Poisson equation was solved using the Euler−Cauchy algorithms,[45] and the discrete electron density was converted to a continuous function using cubic-spline interpolation with natural boundary conditions.

We also compared this time-dependent Poisson approach to the constant (time-independent) potential model defined by the following Yukawa-type screening equation:

$$\psi = \psi_0 \exp(-\gamma(r_s - r)) \quad (5)$$

where the screening γ is equal to 0.5 Å^{-1} and the surface potential is given by the quasi-Nernst formula as above.

RESULTS

Electron Injection and Recombination in Dye-Sensitized Ferrihydrite. Figure 2 compares optical TA spectroscopy and kinetics from dissolved (unbound) 27DCF and 27DCF-sensitized ferrihydrite nanoparticles. These data confirm that TA experiments can follow the photoexcitation, interfacial electron transfer, and recombination processes.[35] At ∼0.2 ps after photoexcitation, both bound and free 27DCF exhibit a new excited-state absorption with a maximum at ∼418 nm. The lifetime of this feature is on the nanosecond time scale for free 27DCF but is lost within 0.5 ps for 27DCF-sensitized FHyd as a result of electron injection. A distinct absorption feature peaked at 447 nm is evident at this time point and is attributed to the oxidized dye that remains bound to the surface, following interfacial electron transfer into nanoparticles.[35,46] As shown in panels B and C of Figure 2, the 447 nm signal is lost as electrons return to the oxidized dye molecules but a fraction of this signal remains beyond 7 ns. The negative-going contribution from 450 to 550 nm represents the loss in the ground-state absorption of the bound dye (termed ground-state bleaching).

Free electrons in iron oxide nanoparticles do not exhibit a strong UV−vis signature,[47] and thus, we used information from the dye transient spectra to track the recombination process. Specifically, we used the strength of the oxidized dye absorption at 447 nm as a measure of the number of electrons remaining within the nanoparticles. We found no detectable differences in the electron injection and recombination kinetics for the two fluorescein derivatives used in this work. Holes generated by bandgap absorption contribute a new UV−vis signal with a maximum at ∼580 nm but decay by electron−hole recombination on a sub-nanosecond time scale.[35]

Figure 3 shows the kinetics of the recombination process from the picosecond to microsecond time scales. The signal of the oxidized dye at 447 nm shows a monotonic decline from 0.2 to 0.002 mOD over 10 μs. This is in agreement our prior work that indicated that the vast majority of photoinjected electrons

DOI: 10.1021/acsearthspacechem.7b00030
ACS Earth Space Chem. XXXX, XXX, XXX−XXX

returned to the donor dye and only ca. 1/300 was lost via Fe^{2+} release into solution.[19] The kinetics data could be fit with a combination of sub-nanosecond exponential functions to account for the picosecond−nanosecond response and a single stretched exponential function for the microsecond−millisecond response.

Lattice MC Simulations of Electron Mobility and Recombination. Figure 4 summarizes the predictions of the lattice MC simulations that were performed to investigate long time scale trapping of polaronic electrons transferred along the iron sublattice in a model nanoparticle. The MC simulations showed fast and slow regimes of electron loss, which qualitatively reproduced the kinetics data (e.g., Figure 3a). The loss of the electron polaron signal over two distinct time scales was most clearly reproduced when the initial electron distribution was segregated to near-surface sites rather than randomly throughout the nanoparticle. This supports a model in which electrons donated by the dye molecules are initially accepted by surface iron sites and electron migration into the nanoparticle subsequently competes with recombination.[19]

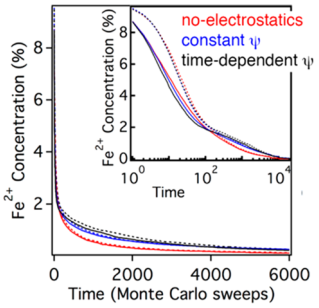

Figure 4. Summary of lattice MC simulations of the distribution of ferrous iron sites introduced in a model nanoparticle and their loss through recombination with surface dye sites. The Fe^{2+} sites were initially distributed randomly among either (i) all lattice sites (dashed lines) or (ii) only subsurface sites (solid lines). Three models for the internal electrostatic potential, $\psi(r)$, were compared to evaluate this influence on Fe^{2+} mobility: (i) no surface potential (red lines), (ii) a constant surface potential (blue lines), or (iii) a time-dependent potential (black lines) obtained by solving the Poisson equation on-the-fly, including the instantaneous distribution of interior electrons. Results show the time dependence of the interior Fe^{2+} concentration for the six cases, displayed on linear and logarithmic (inset) MC time axes. In all cases, the Fe^{2+} decay shows two distinct kinetic regimes, but a more distinct biphasic decay is evident for the initially subsurface distributed Fe^{2+}. For these simulations, Fe^{2+} sites exhibit longer transient lifetimes when the electrostatic calculations of site electron affinities use the time-dependent model.

The longest retention times were obtained for simulations that incorporated a positive surface charge and that recalculated the internal electrostatic potential at every time step based on the instantaneous electron distribution. Inspection of the trajectories of electrons revealed a striking phenomenon of the accumulation of electrons near the surface in simulations incorporating electrostatic field effects. This effect extended the lifetime of all injected electrons through two mechanisms. First, a positive surface potential restricted the mobility of near-surface electrons. Second, electrons that accumulated at the surface electrostatically blocked the access of other more internal electrons to the surface, thereby limiting impingement and recombination at exit channels.

Tests of Physical and Chemical Effects on Recombination Rates. The simulations suggested two testable predictions. First, if internalization occurs through random electron hopping among internal iron sites, recombination should show a dependence upon the particle size. Second, if electrostatic biasing of electron trajectories leads to accumulation in near-surface regions, recombination should show a dependence upon surface charge. We performed TA studies of recombination rates as a function of physical and chemical parameters and quantified the recombination rates using a single stretched exponential decay function, varying the stretching exponent, β, while fixing the time constant, τ, at 0.1 μs, as described above.

Effect of the Nanoparticle Size. A model in which internal electrons propagate freely among all iron sites in a nanoparticle predicts that larger particles would trap electrons over longer time scales than smaller particles. However, as shown in Figure 5, there was a negligible effect of the particle size on the microsecond time scale recombination rates for 27DCF on ferrihydrite nanoparticles. Fits to the data indicate a slight increase in β with an increasing particle size, although this is not statistically significant. This would correspond to a narrowing in the distribution of electron recombination times and a reduction in the longest lifetimes.

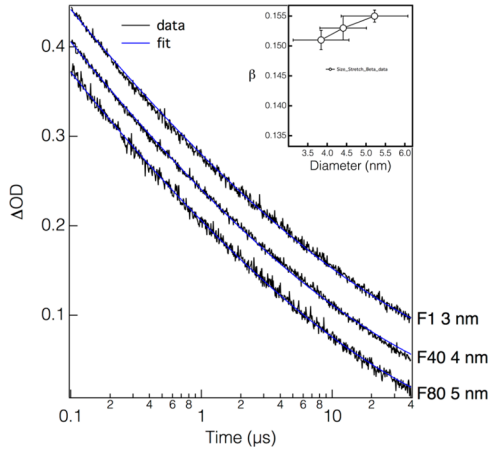

Figure 5. TA kinetic traces at 447 nm for 27DCF bound to three sizes of six-line ferrihydrite nanoparticles. Data (black lines) were collected via TA spectroscopy and fit with a single stretched exponential (blue lines) using a fixed time constant, τ, and a varied stretching parameter, β. The traces are offset vertically for clarity. (Inset) Plot of fitted β and errors (1 standard deviation). The increase of β with the particle size is not statistically significant.

Effect of the Solution pH. Our model predicted that internal electrons are attracted to and trapped by positively charged surface sites. This suggests that recombination would exhibit a dependence upon solution pH, which should control the field strength of the corresponding space charge layer from the surface into nanoparticles.[48] We studied CDCF-sensitized nanoparticles from pH 2.9 to 5.5, which represents a significant change in surface charge density.[37] This range also substantially overlaps the pH range over which iron(II) release from colloidal hematite following pulse radiolysis increased from 0 to 100%.[24] However, as shown in Figure 6, the TA data showed no clear change in microsecond recombination kinetics as a function of solution pH. Nevertheless, after fitting the data with a stretched exponential, a statistically significant increase in β with pH was revealed.

DOI: 10.1021/acsearthspacechem.7b00030
ACS Earth Space Chem. XXXX, XXX, XXX−XXX

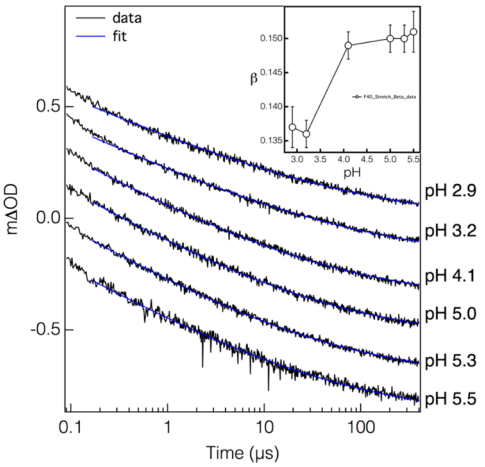

Figure 6. TA kinetic traces at 447 nm for CDCF bound to FHyd40 (4 nm) nanoparticles at different values of solution pH. Data (black lines) were fit with a single stretched exponential (blue lines) using a fixed time constant, τ, and a varied stretching parameter, β. The traces are offset vertically for clarity. (Inset) Plot of fitted β and errors (1 standard deviation). β increased with increasing pH.

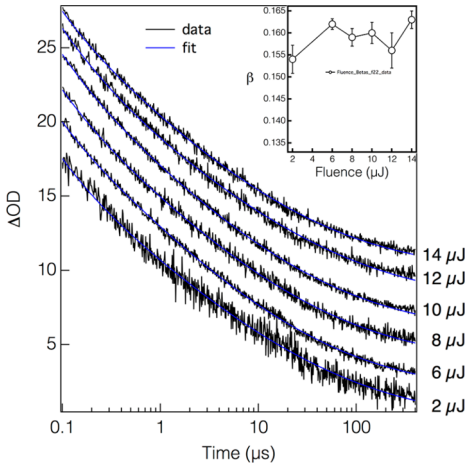

Figure 8. TA kinetic traces at 447 nm for CDCF bound to 4 nm FHyd nanoparticles at pH 4 and high coverage and varying laser pulse energy. Data (black lines) were fit with a single stretched exponential (blue lines) using a fixed time constant, τ, and a varied stretching parameter, β. The traces are offset vertically for clarity. (Inset) Plot of fitted β and errors (1 standard deviation). β did not show a trend with laser power.

Effect of the Number of Injected Electrons. If the internal electrons interact electrostatically with each other, we would expect a dependence of the recombination rate with laser pump power. As shown in Figure 7, we calculated that changing the pump power could alter the mean number of injected electrons per nanoparticle for CDCF bound to ferrihydrite. However, as shown in Figure 8, pump power did not influence the measured recombination kinetics. Fits to the data did not reveal any trend.

Effect of the Nanoparticle Cluster Formation. All of the data reported here were acquired from stable and optically transparent suspensions with no evidence of aggregation. However, aggregation occurred at high dye loading or at high pH, and prior work has shown that unsensitized ferrihydrite nanoparticles can form stable clusters in optically transparent aqueous suspensions.[29,37] Therefore, we used cryo-TEM to investigate the aggregation state of 27DCF-sensitized nanoparticles (Figure 9) under four dye loading conditions (0−40 dye molecules per ferrihydrite particle). The aggregate size increased monotonically with dye loading. The aggregation state of the nanoparticles did not influence the measured recombination kinetics, and fits to the data did not reveal any trend (Figure 10). The same laser pulse energy was used for all dye-loading experiments, resulting in a greater number of injected electrons when dye-loading increased. However, because we observed no trend in recombination kinetics as a function of the number of electrons injected (Figure 7), we conclude that neither the density of injected electrons nor the aggregation state of the nanoparticles had an effect on recombination kinetics and that electron transport is not affected by long-range interactions across multiple particles.

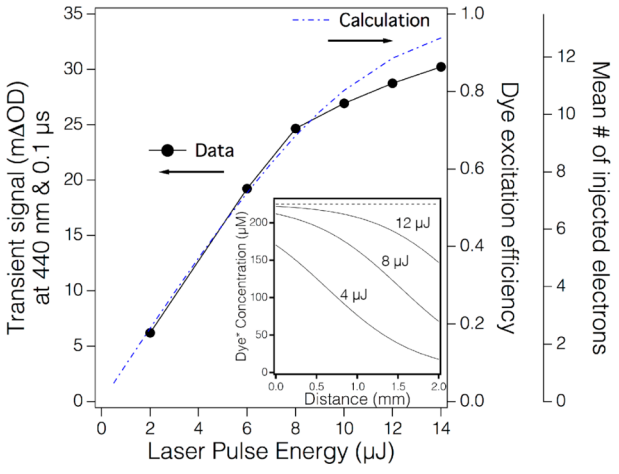

Figure 7. Calculated and observed TA signal from CDCF-sensitized nanoparticles as a function of the laser pulse energy. The data points (plotted versus the left axis) show the TA intensity at 440 nm and 0.1 μs for a high coverage of CDCF on FHyd40. The calculated curve (plotted versus the right axis) shows the single-pulse efficiency of dye photoexcitation, averaged over all molecules in the illuminated volume of a 2 mm cuvette. A value of unity means that all dye molecules were predicted to be photoexcited. Because the dye/nanoparticle concentration ratio was known, the calculated curves also reveal the mean number of injected electrons per nanoparticle (second right axis). (Inset) Calculated curves showing the concentration of photoexcited dye molecules as a function of the laser propagation distance across a 2 mm cuvette for three laser pulse energies.

DISCUSSION

The data show that the nanoparticle size, surface charge, and nanoparticle cluster formation exert small or negligible effects on the rate of recombination in 27DCF- and CDCF-sensitized six-line ferrihydrite nanoparticles. These findings show that the slowest electrons to exit ferrihydrite particles do not exhibit the mobility behavior of an unbiased random walk. Our model predicted that electrostatic trapping of electrons by positive surface sites could dramatically limit electron mobility and, hence, impact a pH dependence to the recombination rate. However, the data show that solution pH exerted a negligible effect on recombination rates, indicating that trapping by protonated surface sites was not significant. A separate mechanism of electrostatic trapping, electron accumulation close to positively charged oxidized dye molecules, cannot be directly assessed by the present experiments. However, prior work showed that recombination can proceed readily, immediately following interfacial electron transfer.[19] This indicates that long-time scale electron retention is enhanced by hopping away

DOI: 10.1021/acsearthspacechem.7b00030
ACS Earth Space Chem. XXXX, XXX, XXX−XXX

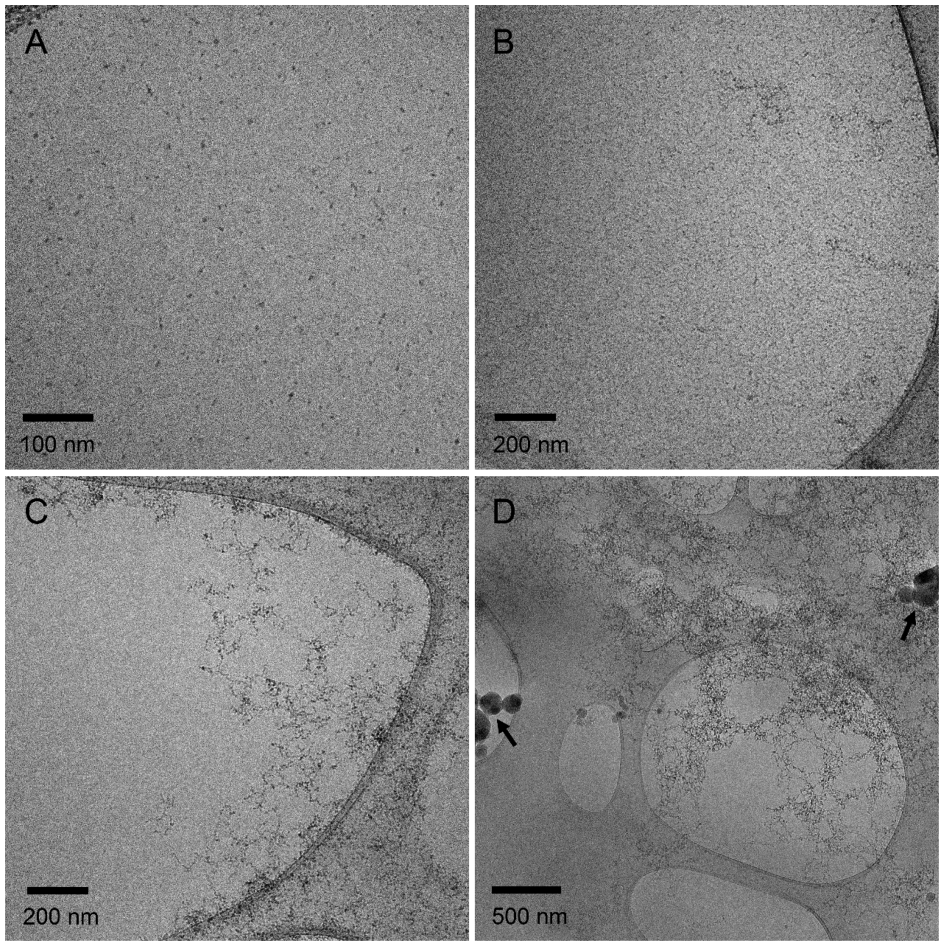

Figure 9. Cryo-TEM images of ferrihydrite nanoparticles with increasing coverage of 27DCF: (A) no dye, (B) 4 dye molecules per ferrihydrite particle, (C) 20 dye molecules per particle, and (D) 40 dye molecules per particle. Black arrows in panel D indicate frost artifacts. Note the changes in scale required to fit larger aggregates within the field of view as dye loading increases.

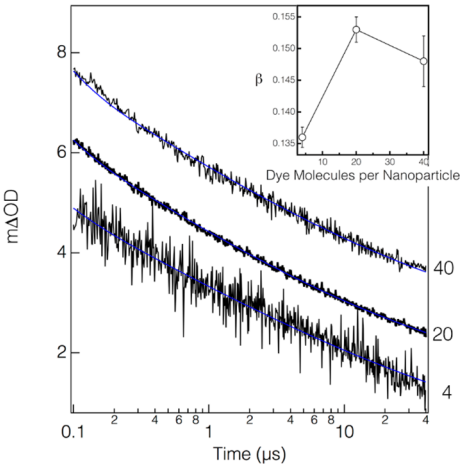

Figure 10. Kinetic traces at 447 nm for DCF bound to FHyd40 (4 nm) nanoparticles at different values of dye coverage (an average of 4, 20, or 40 molecules per nanoparticle). Data (black lines) were fit with a single stretched exponential (blue lines) using a fixed time constant, τ, and a varied stretching parameter, β. The traces are offset vertically for clarity. (Inset) Plot of fitted β and errors (1 standard deviation) as a function of the number of dye molecules per nanoparticle.

from the injection site rather than by electrostatic binding to the oxidized dye.

In conclusion, long-time scale retention of electrons within ferrihydrite is likely caused by slow escape from deep trap states, the rate for which is independent of particle physical characteristics or environmental conditions at the interface. These are likely to be structural defect sites within the nanoparticle, a conclusion in accordance with studies on hematite[49,50] and TiO_2.[51,52] It is very difficult to determine the nature of electron trap sites or to quantify their number and electron affinity. It has been proposed that deep trap sites in hematite are caused by oxygen vacancies.[50,51,53] This is supported by a recent *ab initio* simulation study of Fe(II) adsorbed on goethite showing that surface oxygen vacancies increase the electron affinity of lattice Fe(III) toward accepting (and trapping) the electron from adjacent (adsorbed) Fe(II).[54] However, the stretched exponential form of the best fit recombination function is consistent with a model of trap-limited electron diffusion with a diversity of trap sites.[25,55] With its lack of a definitive structural model,[5,33,56−64] small size, and high surface area/volume ratio, ferrihydrite may have a large number of defect sites. A small particle size and high surface curvature also contribute to undercoordination of surface atoms[65] and strained, high-energy surface structures.[66]

Although we observed very small changes to the recombination rates among all of the samples studied, the data do reveal small trends that suggest new interpretations. For example, Figure 5 shows a weak trend toward faster recombination in the larger nanoparticles, which is counter to the original hypothesis.

DOI: 10.1021/acsearthspacechem.7b00030
ACS Earth Space Chem. XXXX, XXX, XXX−XXX

However, structural analyses showed that six-line ferrihydrite synthesized at a higher temperature to produce larger particle sizes is slightly more crystalline as well. Thus, the trend in Figure 5 could indicate that the density of trap states decreases with an increasing formation temperature and crystallinity. In addition, a decreasing solution pH and an increasing positive surface charge cause a drop in β below pH 4. This could indicate that electron trapping near positively charged surface sites, as hypothesized, does begin to play a more prevalent role at a lower pH than we could explore here. Because this work suggests that electron trap states could act as a significant control on the rates of iron oxide mineral reaction rates, additional work to establish the structural characteristics of these sites is strongly warranted.

CONCLUSION

We observed very minor influences of pH and size on injected electron recombination rates in ferrihydrite nanoparticles and no effect as a result of the nanoparticle aggregation state or the density of injected electrons. Thus, our results indicate that the lowest electron mobilities in ferrihydrite pertain to the rate of escape from deep trap sites. This work has implications for our understanding of the factors controlling the rate of reductive transformation of ferrihydrite. We currently do not know the rate constant for the release of iron(II) from the surface of any iron(III) oxide. Because the lifetime of electrons in deep trap states can enter the microsecond regime, it is plausible that internal electron mobility rather than iron(II) release is the rate-limiting step in reductive dissolution. An important goal of future work will be testing whether electrons are more mobile in different phases of iron oxide that may contain fewer defects and, hence, fewer deep trap sites.

AUTHOR INFORMATION

Corresponding Authors

*E-mail: kevin.rosso@pnnl.gov.
*E-mail: bgilbert@lbl.gov.

ORCID

Adam M. Schwartzberg: 0000-0001-6335-0719
Piotr Zarzycki: 0000-0003-3891-7159
R. Lee Penn: 0000-0002-9610-9507
Kevin M. Rosso: 0000-0002-8474-7720

Notes

The authors declare no competing financial interest.

ACKNOWLEDGMENTS

Benjamin Gilbert was supported by the Office of Science, Office of Basic Energy Sciences (BES), United States Department of Energy (DOE), under Contract DE-AC02-05CH11231. Kevin M. Rosso was supported by the Chemical Sciences, Geosciences, and Biosciences Division, BES, DOE, through the Geosciences Program at Pacific Northwest National Laboratory (PNNL). Jennifer A. Soltis was supported by the University of Minnesota through the Nanostructural Materials and Processes Program, the Department of Chemistry Newman and Lillian Bortnick Fellowship, and the Council of Graduate Students Thesis Research Travel Grant. Jennifer A. Soltis and R. Lee Penn were also supported by the National Science Foundation (NSF, 0957696). Piotr Zarzycki was supported by the National Science Center (DEC-2016/22/E/ST4/00446). The TA studies were performed at the Molecular Foundry, Lawrence Berkeley National Laboratory, which is supported by BES, DOE, under Contract DE-AC02-05CH11231. The cryo-TEM studies were carried out in the Characterization Facility, University of Minnesota, a member of the NSF-funded Materials Research Facilities Network (www.mrfn.org) via the Material Research Science and Engineering Center (MRSEC) program. A portion of this research was performed using Environmental Molecular Sciences Laboratory (EMSL), a national scientific user facility sponsored by the Office of Biological and Environmental Research, DOE, and located at PNNL.

REFERENCES

(1) Jambor, J. L.; Dutrizac, J. E. Occurrence and constitution of natural and synthetic ferrihydrite, a widespread iron oxyhydroxide. *Chem. Rev.* **1998**, *98* (7), 2549−2586.

(2) Cornell, R. M.; Schwertmann, U. *The Iron Oxides: Structures, Properties, Reactions, Occurrences and Uses*, 2nd ed.; Wiley-VCH: Weinheim, Germany, 2003; pp 664.

(3) Hochella, M. F.; Lower, S. K.; Maurice, P. A.; Penn, R. L.; Sahai, N.; Sparks, D. L.; Twining, B. S. Nanominerals, mineral nanoparticles, and earth systems. *Science* **2008**, *319* (5870), 1631−1635.

(4) Stumm, W.; Sulzberger, B. The cycling of iron in natural environments: Considerations based on laboratory studies of heterogeneous redox processes. *Geochim. Cosmochim. Acta* **1992**, *56*, 3233−3257.

(5) Cismasu, A. C.; Michel, F. M.; Tcaciuc, A. P.; Tyliszczak, T.; Brown, G. E., Jr. Composition and structural aspects of naturally occurring ferrihydrite. *C. R. Geosci.* **2011**, *343* (2−3), 210−218.

(6) Casiot, C.; Lebrun, S.; Morin, G.; Bruneel, O.; Personne, J. C.; Elbaz-Poulichet, F. Sorption and redox processes controlling arsenic fate and transport in a stream impacted by acid mine drainage. *Sci. Total Environ.* **2005**, *347*, 122−130.

(7) Jessen, S.; Larsen, F.; Koch, C. B.; Arvin, E. Sorption and desorption of arsenic to ferrihydrite in a sand filter. *Environ. Sci. Technol.* **2005**, *39*, 8045−8051.

(8) Shaw, J. N. Iron and aluminum oxide characterization for highly-weathered Alabama ultisols. *Commun. Soil Sci. Plant Anal.* **2001**, *32*, 49−64.

(9) Rancourt, D. G.; Fortin, D.; Pichler, T.; Thibault, P.-J.; Lamarche, G.; Morris, R. V.; Mercier, P. H. J. Mineralogy of a natural As-rich hydrous ferric oxide coprecipitate formed by mixing of hydrothermal fluid and seawater: Implications regarding surface complexation and color banding in ferrihydrite deposits. *Am. Mineral.* **2001**, *86*, 834−851.

(10) Smedley, P. L.; Kinniburgh, D. G. A review of the source, behavior and distribution of arsenic in natural waters. *Appl. Geochem.* **2002**, *17*, 517−568.

(11) Pichler, T.; Veizer, J.; Hall, G. E. M. Natural input of arsenic into a coral-reef ecosystem by hydrothermal fluids and its removal by Fe(II) oxyhydroxides. *Environ. Sci. Technol.* **1999**, *33*, 1373−1377.

(12) Masue-Slowey, Y.; Loeppert, R. H.; Fendorf, S. Alteration of ferrihydrite reductive dissolution and transformation by adsorbed As and structural Al: Implications for As retention. *Geochim. Cosmochim. Acta* **2011**, *75* (3), 870−886.

(13) Erbs, J. J.; Berquó, T. S.; Reinsch, B. C.; Lowry, G. V.; Banerjee, S. K.; Penn, R. L. Reductive dissolution of arsenic-bearing ferrihydrite. *Geochim. Cosmochim. Acta* **2010**, *74* (12), 3382−3395.

(14) Erbs, J.; Gilbert, B.; Penn, R. L. Influence of size on reductive dissolution of six-line ferrihydrite. *J. Phys. Chem. C* **2008**, *112*, 12127−12133.

(15) Suter, D.; Banwart, S.; Stumm, W. Dissolution of hydrous iron(III) oxides by reductive mechanisms. *Langmuir* **1991**, *7*, 809−813.

(16) Jentzsch, T.; Penn, R. L. Influence of aluminum doping on ferrihydrite nanoparticle reactivity. *J. Phys. Chem. B* **2006**, *110*, 11746−11750.

(17) Jentzsch, T. L. Reactivity of aluminum-doped iron oxide nanoparticles. Ph.D. Thesis, University of Minnesota, Minneapolis, MN, 2007.

(18) Paige, C. R.; Snodgrass, W. J.; Nicholson, R. V.; Scharer, J. M. An arsenate effect on ferrihydrite dissolution kinetics under acidic oxic conditions. *Water Res.* **1997**, *31* (9), 2370−2382.

DOI: 10.1021/acsearthspacechem.7b00030
ACS Earth Space Chem. XXXX, XXX, XXX−XXX

(19) Katz, J. E.; Zhang, X.; Attenkofer, K.; Chapman, K. W.; Frandsen, C.; Zarzycki, P.; Rosso, K. M.; Falcone, R. W.; Waychunas, G. A.; Gilbert, B. Electron small polarons and their mobility in iron (oxyhydr)oxide nanoparticles. *Science* **2012**, *337* (6099), 1200−1203.
(20) Cwiertny, D. M.; Handler, R. M.; Schaefer, M. V.; Grassian, V. H.; Scherer, M. M. Interpreting nanoscale size-effects in aggregated Fe-oxide suspensions: Reaction of Fe(II) with goethite. *Geochim. Cosmochim. Acta* **2008**, *72* (5), 1365−1380.
(21) Gorski, C. A.; Handler, R. M.; Beard, B. L.; Pasakarnis, T.; Johnson, C. M.; Scherer, M. M. Fe atom exchange between aqueous Fe^{2+} and magnetite. *Environ. Sci. Technol.* **2012**, *46* (22), 12399−12407.
(22) Handler, R. M.; Beard, B. L.; Johnson, C. M.; Scherer, M. M. Atom exchange between aqueous Fe(II) and goethite: An Fe isotope tracer study. *Environ. Sci. Technol.* **2009**, *43* (4), 1102−1107.
(23) Yanina, S. V.; Rosso, K. M. Linked reactivity at mineral-water interfaces through bulk crystal conduction. *Science* **2008**, *320* (5873), 218−222.
(24) Mulvaney, P.; Swayambunathan, V.; Grieser, F.; Meisel, D. Dynamics of interfacial charge transfer in iron(III) oxide colloids. *J. Phys. Chem.* **1988**, *92*, 6732−6740.
(25) Nelson, J. Continuous-time random-walk model of electron transport in nanocrystalline TiO_2 electrodes. *Phys. Rev. B: Condens. Matter Mater. Phys.* **1999**, *59*, 15374−15380.
(26) Burleson, D. J.; Penn, R. L. Two-step growth of goethite from ferrihydrite. *Langmuir* **2006**, *22* (1), 402−409.
(27) Burrows, N. D.; Hale, C. R. H.; Penn, R. L. Effect of ionic strength on the kinetics of crystal growth by oriented aggregation. *Cryst. Growth Des.* **2012**, *12* (10), 4787−4797.
(28) Burrows, N. D.; Hale, C. R. H.; Penn, R. L. Effect of pH on the kinetics of crystal growth by oriented aggregation. *Cryst. Growth Des.* **2013**, *13* (8), 3396−3403.
(29) Yuwono, V.; Burrows, N. D.; Soltis, J. A.; Penn, R. L. Oriented aggregation: Formation and transformation of mesocrystal intermediates revealed. *J. Am. Chem. Soc.* **2010**, *132*, 2163−2165.
(30) Yuwono, V. M.; Burrows, N. D.; Soltis, J. A.; Anh Do, T.; Lee Penn, R. Aggregation of ferrihydrite nanoparticles in aqueous systems. *Faraday Discuss.* **2012**, *159* (1), 235−245.
(31) Berquó, T. S.; Erbs, J. J.; Lindquist, A.; Penn, R. L.; Banerjee, S. K. Effects of magnetic interactions in antiferromagnetic ferrihydrite particles. *J. Phys.: Condens. Matter* **2009**, *21* (17), 176005.
(32) Erbs, J. J.; Gilbert, B.; Penn, R. L. Influence of size on reductive dissolution of six-line ferrihydrite–supporting information. *J. Phys. Chem. C* **2008**, *112* (32), 12127−12133.
(33) Gilbert, B.; Erbs, J. J.; Penn, R. L.; Petkov, V.; Spagnoli, D.; Waychunas, G. A. A disordered nanoparticle model for 6-line ferrihydrite. *Am. Mineral.* **2013**, *98* (8−9), 1465−1476.
(34) Guyodo, Y.; Banerjee, S.; Leepenn, R.; Burleson, D.; Berquo, T.; Seda, T.; Solheid, P. Magnetic properties of synthetic six-line ferrihydrite nanoparticles. *Phys. Earth Planet. Inter.* **2006**, *154* (3−4), 222−233.
(35) Gilbert, B.; Katz, J. E.; Huse, N.; Zhang, X.; Frandsen, C.; Falcone, R. W.; Waychunas, G. A. Ultrafast electron and energy transfer in dye-sensitized iron oxide and oxyhydroxide nanoparticles. *Phys. Chem. Chem. Phys.* **2013**, *15* (40), 17303−17313.
(36) Zarzycki, P.; Rosso, K. M. Origin of two time-scale regimes in potentiometric titration of metal oxides. A replica kinetic Monte Carlo study. *Langmuir* **2009**, *25* (12), 6841−6848.
(37) Gilbert, B.; Lu, G. P.; Kim, C. S. Stable cluster formation in aqueous suspensions of iron oxyhydroxide nanoparticles. *J. Colloid Interface Sci.* **2007**, *313* (1), 152−159.
(38) Rasband, W. S. *ImageJ*; National Institutes of Health (NIH): Bethesda, MD, 1997.
(39) Penn, R. L.; Erbs, J.; Gulliver, D. Controlled growth of α-FeOOH nanorods by exploiting-oriented aggregation. *J. Cryst. Growth* **2006**, *293* (1), 1−4.
(40) Pendlebury, S. R.; Barroso, M.; Cowan, A. J.; Sivula, K.; Tang, J.; Gratzel, M.; Klug, D.; Durrant, J. R. Dynamics of photogenerated holes in nanocrystalline α-Fe_2O_3 electrodes for water oxidation probed by transient absorption spectroscopy. *Chem. Commun. (Cambridge, U. K.)* **2011**, *47* (2), 716−718.
(41) Wang, C.-y.; Böttcher, C.; Bahnemann, D. W.; Dohrmann, J. K. A comparative study of nanometer sized Fe(III)-doped TiO_2 photocatalysts: Synthesis, characterization and activity. *J. Mater. Chem.* **2003**, *13* (9), 2322−2329.
(42) Johnston, D. C. Stretched exponential relaxation arising from a continuous sum of exponential decays. *Phys. Rev. B: Condens. Matter Mater. Phys.* **2006**, *74* (18), 184430.
(43) Zarzycki, P.; Charmas, R.; Szabelski, P. Study of proton adsorption at heterogeneous oxide/electrolyte interface. Prediction of the surface potential using Monte Carlo simulations and 1-pK approach. *J. Comput. Chem.* **2004**, *25*, 704−711.
(44) Zarzycki, P.; Rosso, K. M. Nonlinear response of the surface electrostatic potential formed at metal oxide/electrolyte interfaces. A Monte Carlo simulation study. *J. Colloid Interface Sci.* **2010**, *341*, 143−152.
(45) Press, W. H.; Teukolsky, S. A.; Vetterling, W. T.; Flannery, B. P. *Numerical Recipes. The Art of Scientific Computing*, 3rd ed.; Cambridge University Press: New York, 2007.
(46) Hilgendorff, M.; Sundström, V. Dynamics of electron injection and recombination in dye-sensitized TiO_2 particles. *J. Phys. Chem. B* **1998**, *102*, 10505−10514.
(47) Huang, Z.; Lin, Y.; Xiang, X.; Rodriguez-Cordoba, W.; McDonald, K. J.; Hagen, K. S.; Choi, K.-S.; Brunschwig, B. S.; Musaev, D. G.; Hill, C. L.; Wang, D.; Lian, T. Q. *In situ* probe of photocarrier dynamics in water-splitting hematite (α-Fe_2O_3) electrodes. *Energy Environ. Sci.* **2012**, *5*, 8923−8926.
(48) Brown, G. E., Jr.; Henrich, V. E.; Casey, W. H.; Clark, D. L.; Eggleston, C.; Felmy, A.; Goodman, D. W.; Grätzel, M.; Maciel, G.; McCarthy, M. I.; Nealson, K. H.; Sverjensky, D. A.; Toney, M. F.; Zachara, J. M. Metal oxide surfaces and their interactions with aqueous solutions and microbial organisms. *Chem. Rev.* **1999**, *99* (1), 77−174.
(49) Kerisit, S.; Rosso, K. M. Kinetic Monte Carlo model of charge transport in hematite (α-Fe_2O_3). *J. Chem. Phys.* **2007**, *127* (12), 124706.
(50) Barroso, M.; Pendlebury, S. R.; Cowan, A. J.; Durrant, J. R. Charge carrier trapping, recombination and transfer in hematite (α-Fe_2O_3) water splitting photoanodes. *Chem. Sci.* **2013**, *4* (7), 2724−2734.
(51) McNeil, I. J.; Ashford, D. L.; Luo, H.; Fecko, C. J. Power-law kinetics in the photoluminescence of dye-sensitized nanoparticle films: Implications for electron injection and charge transport. *J. Phys. Chem. C* **2012**, *116* (30), 15888−15899.
(52) Kay, A.; Humphry-Baker, R.; Graetzel, M. Artificial photosynthesis. 2. Investigations on the mechanism of photosensitization of nanocrystalline TiO_2 solar cells by chlorophyll derivatives. *J. Phys. Chem.* **1994**, *98* (3), 952−959.
(53) Cherepy, N. J.; Liston, D. B.; Lovejoy, J. A.; Deng, H.; Zhang, J. Z. Ultrafast studies of photoexcited electron dynamics in γ- and α-Fe_2O_3 semiconductor nanoparticles. *J. Phys. Chem. B* **1998**, *102* (5), 770−776.
(54) Alexandrov, V.; Rosso, K. M. Insights into the mechanism of Fe(II) adsorption and oxidation at Fe−clay mineral surfaces from first-principles calculations. *J. Phys. Chem. C* **2013**, *117* (44), 22880−22886.
(55) Berben, D.; Buse, K.; Wevering, S.; Herth, P.; Imlau, M.; Woike, T. Lifetime of small polarons in iron-doped lithium−niobate crystals. *J. Appl. Phys.* **2000**, *87*, 1034−1041.
(56) Eggleton, R. A.; Fitzpatrick, R. W. New data and a revised structural model for ferrihydrite. *Clays Clay Miner.* **1988**, *36* (2), 111−124.
(57) Drits, V. A.; Sakharov, B. A.; Salyn, A. L.; Manceau, A. Structural model for ferrihydrite. *Clay Miner.* **1993**, *28* (2), 185−207.
(58) Rancourt, D. G.; Meunier, J. F. Constraints on structural models of ferrihydrite as a nanocrystalline material. *Am. Mineral.* **2008**, *93* (8−9), 1412−1417.
(59) Harrington, R.; Hausner, D. B.; Xu, W.; Bhandari, N.; Michel, F. M.; Brown, G. E., Jr.; Strongin, D. R.; Parise, J. B. Neutron pair distribution function study of two-line ferrihydrite. *Environ. Sci. Technol.* **2011**, *45* (23), 9883−9890.
(60) Manceau, A. Critical evaluation of the revised akdalaite model for ferrihydrite. *Am. Mineral.* **2011**, *96*, 521−533.

DOI: 10.1021/acsearthspacechem.7b00030
ACS Earth Space Chem. XXXX, XXX, XXX−XXX

(61) Manceau, A.; Skanthakumar, S.; Soderholm, L. PDF analysis of ferrihydrite: Critical assessment of the under-constrained akdalaite model. *Am. Mineral.* **2014**, *99* (1), 102−108.
(62) Michel, F. M.; Ehm, L.; Antao, S. M.; Lee, P. L.; Chupas, P. J.; Liu, G.; Strongin, D. R.; Schoonen, M. A. A.; Phillips, B. L.; Parise, J. B. The Structure of ferrihydrite, a nanocrystalline material. *Science* **2007**, *316* (5832), 1726−1729.
(63) Michel, F. M.; Barron, V.; Torrent, J.; Morales, M. P.; Serna, C. J.; Boily, J. F.; Liu, Q.; Ambrosini, A.; Cismasu, A. C.; Brown, G. E. Ordered ferrimagnetic form of ferrihydrite reveals links among structure, composition, and magnetism. *Proc. Natl. Acad. Sci. U. S. A.* **2010**, *107* (7), 2787−2792.
(64) Penn, R. L. CHEMISTRY: Resolving an Elusive Structure. *Science* **2007**, *316* (5832), 1704−1705.
(65) Abbas, Z.; Labbez, C.; Nordholm, S.; Ahlberg, E. Size-dependent surface charging of nanoparticles. *J. Phys. Chem. C* **2008**, *112*, 5715−5723.
(66) Zhang, H.; Penn, R. L.; Hamers, R. J.; Banfield, J. F. Enhanced adsorption of molecules on surfaces of nanocrystalline particles. *J. Phys. Chem. B* **1999**, *103*, 4656−4662.

DOI: 10.1021/acsearthspacechem.7b00030
ACS Earth Space Chem. XXXX, XXX, XXX−XXX